

PAPER • OPEN ACCESS

Femtosecond laser-induced nanoparticle implantation into flexible substrate for sensitive and reusable microfluidics SERS detection

To cite this article: Yongxiang Hu *et al* 2024 *Int. J. Extrem. Manuf.* **6** 045005

View the [article online](#) for updates and enhancements.

You may also like

- [Nanowire assisted repeatable DEP-SERS detection in microfluidics](#)
Tingting Ge, Sheng Yan, Lingjun Zhang et al.
- [Silver nanoparticle-assembled micro-bowl arrays for sensitive SERS detection of pesticide residue](#)
Chuhong Zhu, Qiangsheng Zhao, Guowen Meng et al.
- [Construction of flexible, transparent and mechanically robust SERS-active substrate with an efficient spin coating method for rapid *in-situ* target molecules detection](#)
Feng Bai, Jinchun Dong, Jianbo Qu et al.

Femtosecond laser-induced nanoparticle implantation into flexible substrate for sensitive and reusable microfluidics SERS detection

Yongxiang Hu^{1,4,*} , Yu Zhou^{1,4} , Guohu Luo¹, Dege Li² and Minni Qu³

¹ State Key Laboratory of Mechanical System and Vibration, School of Mechanical Engineering, Shanghai Jiao Tong University, Shanghai 200240, People's Republic of China

² School of Mechanical and Power Engineering, Nanjing Tech University, Nanjing 211816, People's Republic of China

³ Center for Advanced Electronic Materials and Devices, School of Electronic Information and Electrical Engineering, Shanghai Jiao Tong University, Shanghai 200240, People's Republic of China

E-mail: huyx@sjtu.edu.cn

Received 27 December 2023, revised 18 February 2024

Accepted for publication 7 May 2024

Published 24 May 2024



Abstract

Surface-enhanced Raman spectroscopy (SERS) microfluidic system, which enables rapid detection of chemical and biological analytes, offers an effective platform to monitor various food contaminants and disease diagnoses. The efficacy of SERS microfluidic systems is greatly dependent on the sensitivity and reusability of SERS detection substrates to ensure repeated use for prolonged periods. This study proposed a novel process of femtosecond laser nanoparticle array (NPA) implantation to achieve homogeneous forward transfer of gold NPA on a flexible polymer film and accurately integrated it within microfluidic chips for SERS detection. The implanted Au-NPA strips show a remarkable electromagnetic field enhancement with the factor of 9×10^8 during SERS detection of malachite green (MG) solution, achieving a detection limit lower than 10 ppt, far better than most laser-prepared SERS substrates. Furthermore, Au-NPA strips show excellent reusability after several physical and chemical cleaning, because of the robust embedment of laser-implanted NPA in flexible substrates. To demonstrate the performance of Au-NPA, a SERS microfluidic system is built to monitor the online oxidation reaction between MG/NaClO reactants, which helps infer the reaction path. The proposed method of nanoparticle implantation is more effective than the direct laser structuring technique. It provides better performance for SERS detection, robustness of detection, and substrate flexibility and has a wider range of applications for microfluidic systems without any negative impact.

⁴ These authors contributed equally to this work.

* Author to whom any correspondence should be addressed.



Original content from this work may be used under the terms of the [Creative Commons Attribution 4.0 licence](https://creativecommons.org/licenses/by/4.0/). Any further distribution of this work must maintain attribution to the author(s) and the title of the work, journal citation and DOI.

Supplementary material for this article is available [online](#)

Keywords: femtosecond laser-induced transfer, nanoparticle array, surface-enhanced Raman spectrum, microfluidic system

1. Introduction

Surface-enhanced Raman spectroscopy (SERS), as an ultra-sensitive, noninvasive, and effective method, attracts substantial research interest in the label-free detection of bio/chemical analytes [1–3]. Recent days witness the trend to integrate SERS-active nanoparticles or structures into microfluidic chips to broaden their applications in biomedical diagnosis [4], environmental monitoring [5], and food safety [6] in order to make full use of the advantages of microfluidic devices such as high sensitivity, high efficiency, and low cost [7]. Integrating SERS into microfluidic systems also brings some challenges, including how to assemble well-designed plasmonic nanoparticles into microchannels to ensure SERS sensitivity, reproducibility, and reusability.

Integration approaches can be realized by external injection, built-in assembly, and in-situ fabrication [7], but most of them have their pros and cons. For the external injection method, colloidal nanoparticles and analytes are simultaneously injected into microchannels and mixed to enhance the Raman scattering signal, but nanoparticles are prone to aggregate, resulting in lower SERS detection reproducibility [8]. Built-in implantation/assembly method enables a consistent high-resolution and large-scale SERS detection, but this method greatly relies on lithography-based [9, 10] and template-based [11, 12] techniques, suffering from low fabrication efficiency and expensive costs [13], calling for a fast and affordable technique, to which regard laser structuring is a good candidate [14, 15].

Direct laser structuring has been used to develop many high-sensitive microfluidic SERS systems [16], offering various flexible SERS-active interface fabrication routes. For example, using laser-induced photoreduction, nanoparticles can be synthesized in microchannels for SERS detection with resolution as low as 10^{-10} mol l^{-1} [17]. Reduction-produced SERS-active metal substrates can be further modulated by a linear polarized laser to improve SERS sensitivity [18]. Nevertheless, laser-reduced nanoparticles are susceptible to oxidization when exposed to air, which will affect their service lifetime [19]. To broaden the material applicability of laser-produced SERS substrates for reliable microfluidics applications, direct laser scribing [20], laser writing [21] and laser synthesis [22] methods are developed to integrate various materials into microchannels. However, laser-fabricated structures are difficult to be controlled into a homogeneous manner [23, 24], significantly limiting the improvement of SERS sensitivity and reproducibility. Femtosecond laser-induced forward transfer (fs-LIFT) enabling the preparation of a very homogeneous plasmonic nanoparticle array

(NPA) [25] may address this issue. The resolution of fs-LIFT-formed plasmonic particles is as high as 40 nm and the fabrication scale can reach several millimeters, enough to meet large-scale SERS detection applications [26], showing great potential to be a substitute for other-technique built-in Raman-active substrates [27] for microfluidic SERS application explosion after transferring into soft polymers.

In this study, we demonstrated the possibility of implanting the uniform NPAs into a flexible polymer substrate using fs-LIFT for microfluidic SERS detection. The NPA-based SERS strips were developed to detect malachite green (MG) solution using both evaporative and liquid detection methods and to evaluate SERS testing sensitivity and their detection limit. Numerical simulation was conducted to reveal NPA electromagnetic enhancement introduced by surface plasmon resonance, and the corresponding enhancement factor (EF) was calculated. Furthermore, physical and chemical treatments were used repeatedly to evaluate their stability and reusability of as-prepared SERS strips. NPAs were integrated into a microfluidic chip to execute an effective monitor of the in-situ redox reaction. This work aims to prove femtosecond laser nanoparticle implantation to be an accurate, efficient, and flexible approach to integrating SERS-active substrates with microfluidic systems.

2. Materials and methods

2.1. Materials

Quartz glass wafers with a diameter of 10 mm and a thickness of 0.5 mm were purchased from Yuanfeng Quartz Products Co., Ltd. MG ($C_{23}H_{25}ClN_2$) and Sodium hypochlorite aqueous solution (NaClO, 5%) were purchased from Sinopharm Chemical Reagent Co., Ltd. Polydimethylsiloxane (PDMS) film with a thickness of 500 μm was purchased from Zhongke Materials Co., Ltd. Polyethylene terephthalate (PET) film with a thickness of 10 μm was purchased from Toray Industries, Inc.

2.2. Laser-induced implantation

Figure 1(a) illustrates the self-developed fs-LIFT device used for implanting nanoparticles into the flexible substrate. A femtosecond laser system (Light Conversion, PHAROS) was used to generate the laser pulse with a duration of 290 fs, a wavelength of 1030 nm, and linear polarization. The pulse energy could be continuously adjusted with an attenuator (Altechna PowerXP). The laser beam with an initial diameter of 3 mm was focused to 96.2 μm by a convex lens with a

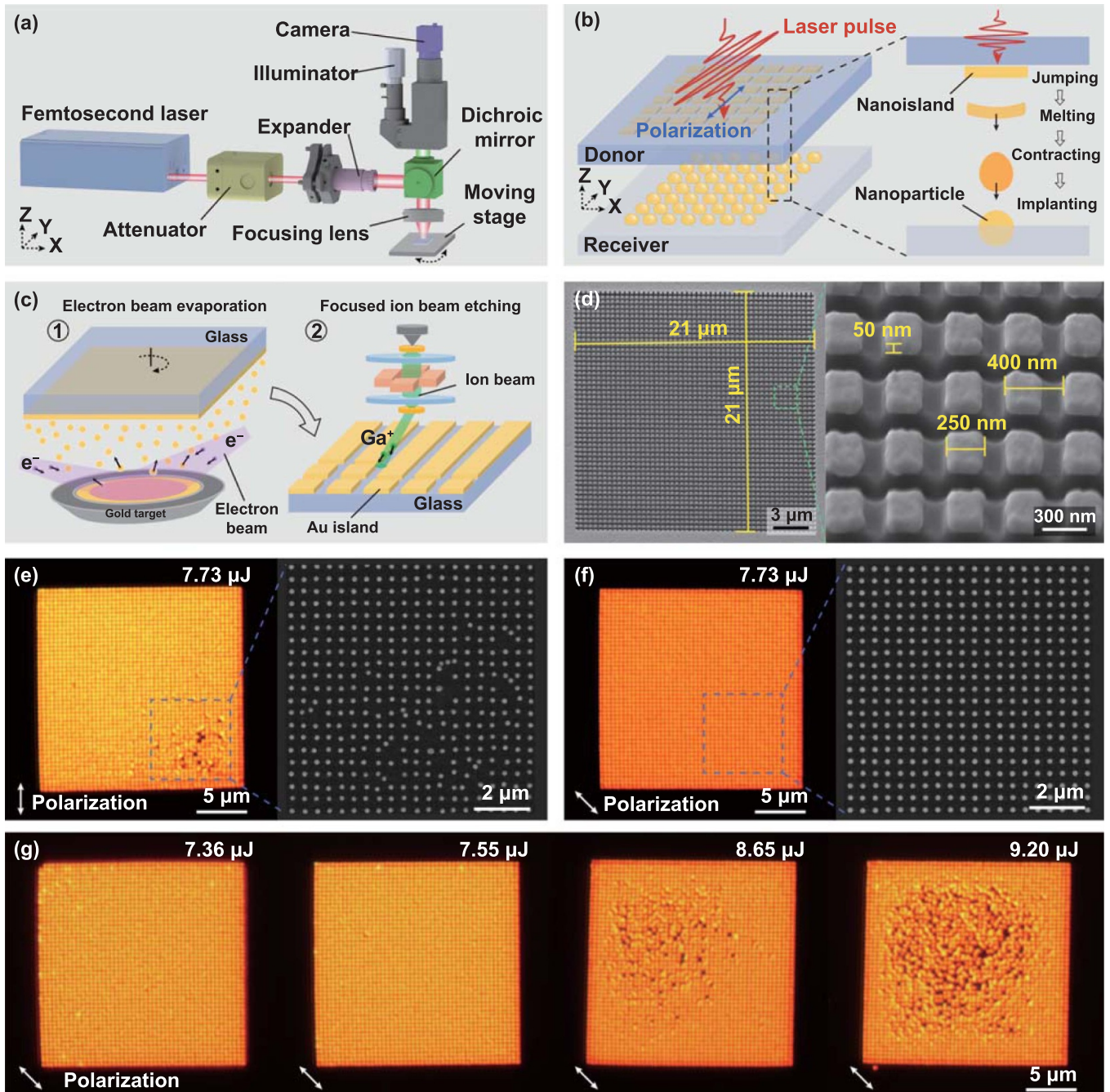


Figure 1. Femtosecond laser implantation of nanoparticle array on a flexible substrate. (a) Experimental device and (b) schematic of the laser-induced forward transfer. (c) Preparation process and (d) SEM image of patterned Au islands on glass. NPAs fabricated under a vertically (e) and (f) diagonally polarized laser pulse. (g) NPAs fabricated using a diagonally polarized laser pulse with different pulse energies.

focal length of 150 mm (THORLABS). The coaxial camera and illuminator were installed after a dichroic mirror for assistance in focusing and positioning. The transparent donor with patterned nanoislands was placed on and in contact with the surface of the flexible receiver. After the laser irradiation, the nanopatterns were transferred onto the flexible receiver, as shown in figure 1(b). The gap distance between the donor and

receiver was controlled on a submicron scale to ensure the fabricating accuracy. A 3-axis moving stage with a repositioning resolution of $<1 \mu\text{m}$ was used to move the sample. The linear polarization of the femtosecond laser is fixed along the vertical (Y) direction. A manual rotating platform was utilized to change the angle between the specimen and the laser polarization.

2.3. Preparation of patterned nanoisland array

Figure 1(c) shows the fabrication process of a patterned gold (Au) nanoisland array on a transparent donor. Au film with a thickness of 50 nm was deposited on the quartz glass using an electron beam evaporation system (Denton Explorer), then etched by a focused ion beam (FIB, Zeiss Auriga) of 30 kV: 120 pA. The etching depth and width were adjusted via the ion dose in the range of $0.4 \text{ nC } \mu\text{m}^{-2} - 0.5 \text{ nC } \mu\text{m}^{-2}$. Here, the etching length, width, and pitch were set to 21 μm , 150 nm, and 400 nm, respectively. Nanoisland array with a side length of 250 nm and scale of 50×50 was obtained to transfer, as shown in figure 1(d). The design of the above array geometry was based on a comprehensive consideration of fs-LIFT process accuracy [28] and SERS detection performance.

2.4. Morphological characterization

The optical images of NPAs were collected by an optical microscope (OLYMPUS) with the 20 \times , 50 \times , and 100 \times objectives. Scanning electron microscopy (SEM, TESCAN MAGNA) was utilized to capture the high-resolution images under the UH-RESOLUTION scan mode with a beam energy of 5 keV and an intensity of 30 pA. The PDMS was sputtered with platinum for 15 s using a sputter coater (Quorum Q150T) to increase the conductivity. The cross-section was cut by FIB with a 30 kV: 20 pA gallium beam. The sectional and oblique images of NPA were taken at a tilted angle of 54 $^\circ$. The atomic force microscope (AFM, Bruker FastScan Bio) was used to scan NPA surface topography, and the AFM data were treated with Gwyddion package.

2.5. Raman spectroscopy

The Raman detections were performed with a confocal Raman microscope (inVia Qontir, RENISHAW) equipped with an excitation laser of 532 nm wavelength and 32 mW peak power (sample surface). The 532 nm wavelength was widely used in the SERS detection of MG [19, 20, 29, 30], making mutual performance comparison possible. The spectral measurement range was set from 500 cm^{-1} to 2000 cm^{-1} via a diffraction grating of 1800 grooves mm^{-1} . The laser power was attenuated to 1% of the maximum. A 50 \times L objective lens (N.A. = 0.5) was adopted to focus a spot with a diameter of about 1.3 μm . The spectra were measured with an exposure time of 1 s and an accumulation count of 10. The raw Raman data were processed using WiRE software.

2.6. Numerical simulation

The optical field enhancement of the Au nanoparticles on PDMS film was calculated by the finite difference time domain (FDTD) simulation. The FDTD model of NPA was simplified into an individual nanoparticle with periodic boundary conditions to save computing resources. The plane wave source was adopted to simulate the Raman laser incidence [31]. The parameters of Au were fitted from the experiment of Johnson and Christy [32]. The refractive index of PDMS was set to

1.43 at 532 nm wavelength [33]. The simulation models were depicted in the supplementary material. The FDTD simulations were conducted using COMSOL software.

2.7. Fabrication of microfluidic chip

The microchannel and microchamber were milled on a 60 mm \times 25 mm \times 2 mm quartz glass. The microchannel was designed with a width of 2 mm and depth of 1 mm, while the through-hole inlets, outlet, and microchamber were also fabricated on the glass plane. After the mechanical processing, the glass plate was thoroughly cleaned with alcohol and deionized water using ultrasonic cleaning. Subsequently, the PDMS substrate implanted with NPAs was bonded onto the glass surface containing the microchannels using oxygen plasma treatment [34].

3. Results and discussion

3.1. Preparation of NPA on flexible film

The nanoparticle implantation on PDMS film was conducted using the fs-LIFT technique (figure 1(a)). After laser irradiation, nanoislands jumped off the donor substrate and were implanted into the flexible film, driven by the ultrafast laser-excited thermal stress [35]. Meanwhile, the nanoislands contracted to spherical nanoparticles because of laser heating, as illustrated in figure 1(b). During this process, PDMS could not be damaged by laser pulse irradiation because its ablation threshold was higher than that of gold film [36, 37]. However, the plasmon resonances during the transfer process caused the inhomogeneous field enhancement at the array edge and severely increased the deposition deviation, as shown in figure 1(e). A polarization-modulated method was developed to tune the reflection of plasmonic resonance waves and improve the uniformity of local field enhancement [28]. The printing accuracy of NPA was significantly improved by tuning the laser polarization, as shown in figure 1(f). Then, the effect of pulse energy on NPA morphology was investigated (figure 1(g)), validating the reproducibility of the proposed method.

The morphology and deviation of the NPA on PDMS film were characterized in detail to evaluate its performance. The surface morphology of the entire array was imaged in figure 2(a). The nanoparticles were arranged in a square lattice with a uniform pitch of about 400 nm, suggesting a high-quality lattice plasmon resonances can be excited, as reported by the previous study [38, 39]. Besides, the zoom-in view in figure 2(b) presents the nanoparticles as a hemisphere, indicating that the particles were partially embedded in PDMS film, which is also confirmed by the sectional view in figure 2(c). Embedding nanoparticles into the flexible film is beneficial to ensure good reliability. The arrangement pitch, position deviation, and embedded depth, which determine the sensing sensitivity and stability, were quantified, respectively. The particle positions were obtained from figure 2(a) via an image processing method. Then, a position-matching algorithm was developed (figure S1) to calculate the arrangement pitch and

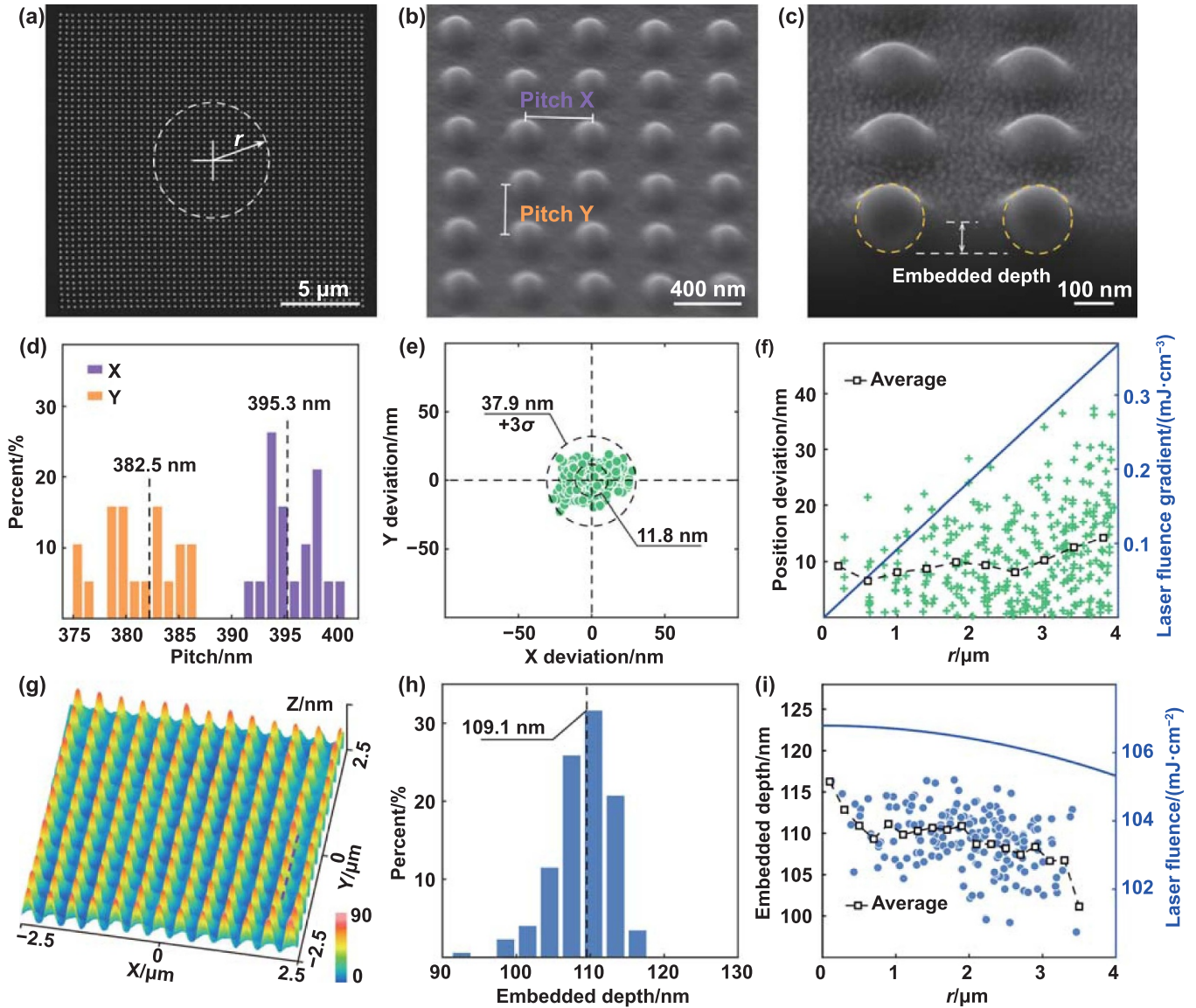


Figure 2. Morphology and deviation of the printed nanoparticle array by tuning laser polarization. (a) SEM image of NPA on PDMS film, (b) Zoom-in view, and (c) sectional view. (d) Arrangement intervals in X and Y directions of nanoparticles. (e) Position deviation and (f) its dependence on the radial distance to the spot center (charted in (a)). The right axis of (f) plots the laser fluence gradient. (g) Surface topography measured by AFM. (h) Embedded depth and (i) its distribution along the radial distance. The right axis of (i) represents the laser fluence.

deviation distribution (a more detailed description is in supplementary note S1). The arrangement pitches along the X and Y directions were 382.5 nm and 395.3 nm, respectively (figure 2(d)). The initial misalignment along the two directions induced by the FIB process was about 1 nm [28]. Therefore, the difference between pitch X and pitch Y is mainly caused by the deformation of the flexible film during the adhesion and peeling processes. As shown in figure 2(e), the mean and maximum position deviations were 11.8 nm and 37.9 nm ($P = 99.73\%$), indicating that the mean deviation was only 3% of the array pitch. The position deviation increases with the radial distance to the spot center figure 2(f), which was in sync with the trend of the laser fluence gradient (right axis in figure 2(f)), and can be explained by the fact that the jumping

behavior of the island is driven by the thermal effect related to the laser fluence gradient [28].

Furthermore, the surface topography measured by AFM exhibited a perfect height consistency as shown in figure 2(g). The mean embedded depth is approximately 109.1 nm and exceeds the particle radius of 90.7 nm (figure 2(h)), indicating more than half of the particle was embedded in PDMS. Moreover, figure 2(i) demonstrates that the embedded depth decreases significantly with the radial distance. The laser fluence decreases along the radical direction for a Gaussian profile (right axis in figure 2(i)), suggesting that the higher laser fluence could result in the increase of embedded depth. However, the excessive depth will weaken the plasmonic enhancement of NPAs. Therefore, the embedded depth can

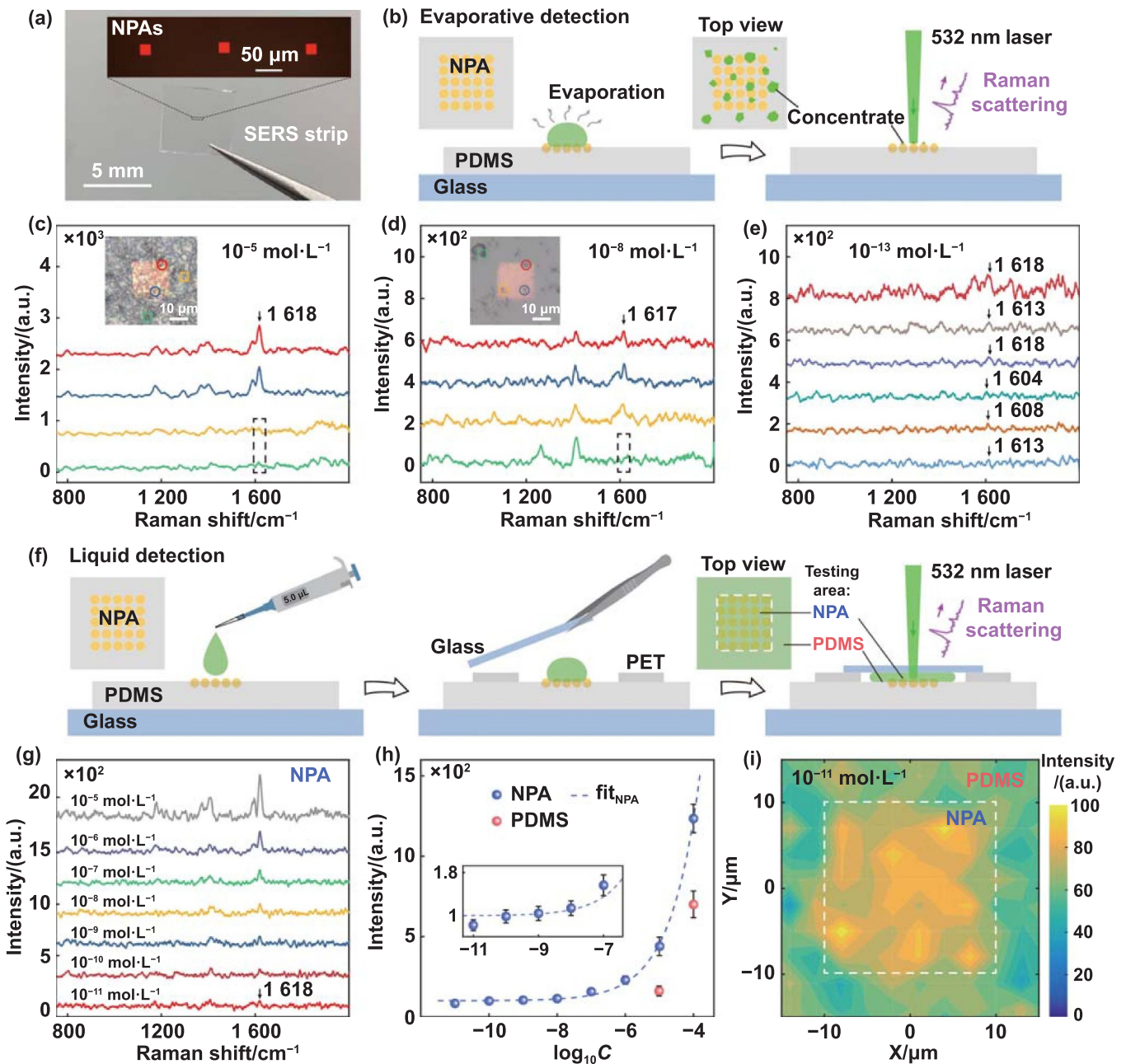


Figure 3. Surface-enhanced Raman scattering detection of low-concentration solution. (a) Test strip with NPAs on PDMS film. (b) Schematic of evaporative detection of low-concentration solution. Raman spectra of (c) 10^{-5} mol·L $^{-1}$, (d) 10^{-8} mol·L $^{-1}$, and (e) 10^{-13} mol·L $^{-1}$ MG solutions measured from different positions of NPA after being concentrated. The insets in (c) and (d) display the concentrates on NPAs, and the detection positions are indicated with different markers. (f) Illustration of a liquid detection process. The inset shows the different test regions in a top view. Raman spectra of MG solution with different concentrations on (g) NPA, measured from liquid directly. (h) Variation of 1619 cm^{-1} peak intensities (charted in (g)) towards logarithmic concentration. (i) Raman mapping (1619 cm^{-1} peak) of 10^{-11} mol·L $^{-1}$ MG solution on NPA and PDMS areas. The scanning step is $3\text{ }\mu\text{m}$ in the X and Y directions.

be precisely controlled by the fluence to achieve a balance between performance and lifetime.

3.2. Electromagnetic enhancement of Raman detection

Test strips were prepared by implanting the NPAs on the PDMS substrate to test their SERS performance, as shown in figure 3(a). The conventional evaporative detection of a low-concentration solution was first adopted to characterize the

SERS sensitively, as illustrated in figure 3(b). The MG solution dropped on the SERS substrate is heated to evaporate and concentrate, then searched and detected by a Raman microscope. The Raman spectra of concentrated 10^{-5} mol·L $^{-1}$, 10^{-8} mol·L $^{-1}$, and 10^{-13} mol·L $^{-1}$ of MG solution are shown in figures 3(c)–(e). The strongest characteristic peak of MG is at 1619 cm^{-1} (figure S2(a)), indicating the different vibrational modes of its phenyl ring [40]. The Raman spectrum of the test strip, composed of PDMS and NPAs, exhibits a peak

Table 1. Comparison in various microfluidic SERS substrates.

Integration methods	Target analytes	LOD	EF	References
External injection of Ag nanoparticles colloid	Malachite green	1 ppb – 2 ppb	—	[41]
Laser-induced coreduction of Ag/Pd alloy nanostructures	Rhodamine 6 G	10^{-9} mol·l ⁻¹	2.6×10^8	[19]
Laser scribing of Ag nanoparticles and graphene oxide composites	Rhodamine 6 G	10^{-10} mol·l ⁻¹	8.9×10^8	[20]
Femtosecond laser direct ablation, selective metallization, and inducing periodic surface structure	Rhodamine 6 G	10 ppb	7.3×10^8	[18]
Direct laser writing micropillars, Au film deposition, and capillary-force driven self-assembly	Rhodamine 6 G	10^{-6} mol·l ⁻¹	8×10^7	[21]
^a Femtosecond laser-induced nanoparticle implantation	Malachite green	10^{-11} mol·l ⁻¹ (3.6 ppt)	9×10^8	This work

^a The LOD of our SERS strip will be further reduced if used to detect rhodamine 6G because the LOD of rhodamine 6G is generally lower than that of MG under the same testing condition [29, 30, 43].

at 1407 cm^{-1} (figure S2(b)). In addition, there is no additional overlap in the Raman spectra of MG and strip. Thus, the 1619 cm^{-1} peak was monitored to confirm the existence of MG. As shown in figure 3(c), the concentrated $10^{-5}\text{ mol}\cdot\text{l}^{-1}$ MG solution could fully cover the NPAs. However, a significant difference in intensity appeared when Raman spectra were used for inside and outside NPA detections. The 1619 cm^{-1} peak of MG on bare PDMS disappears entirely, as indicated by the dotted box in figure 3(c). When the concentration was lowered to $10^{-8}\text{ mol}\cdot\text{l}^{-1}$, only a few MG particles were randomly distributed on the strip (figure 3(d)). The substances on NPA can be detected clearly, while the spectrum acquired on bare PDMS has no characteristic peaks, denoted by the dotted box in figure 3(d). The Raman spectrum of a concentrated $10^{-13}\text{ mol}\cdot\text{l}^{-1}$ solution is presented in figure 3(e). Because of the tiny size and uneven distribution of MG concentrates, the 1619 cm^{-1} peak intensities exhibited a large variation under repeated testing. Moreover, the 1619 cm^{-1} peak overlapped with the 1594 cm^{-1} peak, causing a left shift of the peak position (figure 3(e)). The mean peak intensity decreased to around 90, which is slightly above the testing noise, so we concluded the limit of detection (LOD) of NPA-based SERS strips was $10^{-13}\text{ mol}\cdot\text{l}^{-1}$ (MG) using the evaporative detection method.

The above-described method makes quantifying the solution concentration difficult because of the random distribution of solution concentrate, which inspired us to develop a direct liquid detection method using the NPA strip, as demonstrated in figure 3(f). The PDMS film was attached to a glass slide for easier operation. Two PET tapes with a thickness of $10\text{ }\mu\text{m}$ were stuck on both sides of NPAs. $5\text{ }\mu\text{l}$ solution was then dropped on the SERS strip, and another glass slide was placed on the PET tapes to disperse the droplet evenly on NPAs, which was then used for a Raman test. Figure 3(g) shows the Raman spectra for MG solutions with different concentrations. The intensity of the 1619 cm^{-1} peak declined continuously as the concentration went down. Under this condition, the LOD of MG solution is about $10^{-11}\text{ mol}\cdot\text{l}^{-1}$ (figure S3) and close to 3.6 ppt, much lower than the previous microfluidic SERS substrates [18, 21, 41, 42], as compared in table 1. Moreover,

the LOD of our SERS strip may be further reduced if used to detect rhodamine 6G [29], which was widely used in SERS detections.

The LOD of bare PDMS substrate is only $10^{-5}\text{ mol}\cdot\text{l}^{-1}$ (figure S4). Then, the EF of the liquid detection is calculated as 9×10^8 (a more detailed description is in supplementary note S2). Besides, the liquid detection method notably reduced the assay time of low-concentration solution to only minutes without evaporation and concentration. The most prominent advantage is the ability to quantify the solution concentration due to the uniform field enhancement of NPAs. As shown in figure 3(h), we fitted the dependence of 1619 cm^{-1} peak intensity on the logarithmic concentration C in figure 3(g). The peak intensity I increases exponentially with $\log_{10}C$, which could be perfectly fitted by $I = a \exp(b \log_{10}C) + c$. The fitting coefficients are $a = 1.185 \times 10^5$, $b = 1.163$, $c = 81.04$, respectively. The above approach can assist the Raman test to determine the solution concentration efficiently. As the concentration decreases, the relative standard deviation of the detected peak intensity tends to be 12% (figure S5), consistent with the previous publication [44]. These data suggest the detecting error will not expand further at an ultra-low concentration. In addition, the scanning Raman mapping (1619 cm^{-1} peak) of $10^{-11}\text{ mol}\cdot\text{l}^{-1}$ MG solution exhibited a significant intensity enhancement on NPA compared to bare PDMS substrate without nanoparticle implantation, as shown in figure 3(h). These results demonstrate the high sensitivity and reproducibility of our NPA-based SERS substrate.

The FDTD simulation was conducted to reveal the electromagnetic enhancement of NPA in SERS detection. The particle diameter, embedded depth, and arranged pitch were obtained from figure 2. The flat-top laser beam with a wavelength of 532 nm was adopted to illuminate NPA. The incident laser was linearly polarized along the X direction. The surface distributions of the normalized electric field intensity $|E|^2/|E_0|^2$ were extracted in different planes (illustrated in figure S6) and charted in figures 4(a)–(f). Because of the strong coupling between the adjacent nanoparticles, the incident laser is trapped within the NPA plane, causing the

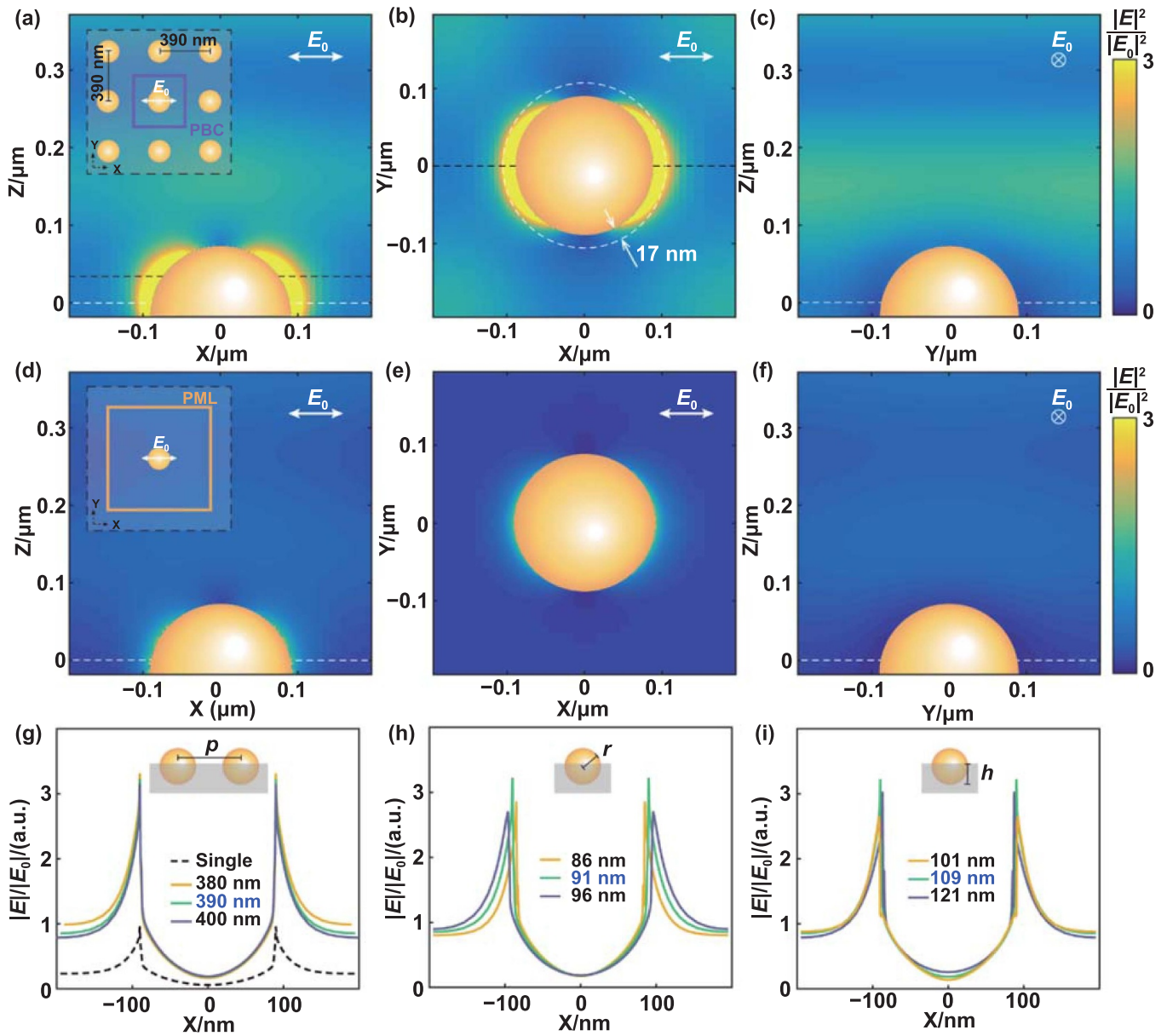


Figure 4. Plasmonic field enhancement of nanoparticle array. Enhanced distribution of normalized electric field intensity $|E|^2/|E_0|^2$ in the (a) XZ, (b) XY, and (c) YZ planes of NPA excited by a 523 nm wavelength and linearly polarized laser. The inset in (a) shows the array geometry. Enhanced distribution of $|E|^2/|E_0|^2$ in the (d) XZ, (e) XY, and (f) YZ planes of a single nanoparticle excited with the same laser source. The inset in (d) exhibits the simulation model. Enhanced field profile $|E|/|E_0|$ along the X axis in XY plane with different (g) arrangement pitches, (h) particle radii, and (i) embedded depths.

significant enhancement of the local optical field near each nanoparticle [9]. The field enhancement was primarily concentrated in the area of more than 10 nm away from the particle surface, as illustrated in figure 4(b). A dipolar lattice mode was exhibited in NPA, which is consistent with the previous studies [38, 39]. Moreover, compared with the perpendicular direction, the field intensity along the polarization direction of the excited laser was stronger (figures 4(a) and (c)). This directionality enhancement has a potential application in the polarized optical spectrum for anisotropic materials [45]. As a comparison, the field enhancement of a single particle also appeared on the particle surface along the polarized direction (figures 4(d)–(f)), but its magnitude is much lower than that

of NPA. These results directly evidence the effect of localized surface plasmon resonance on electromagnetic field enhancement in NPA. When the analyte molecules are adsorbed onto the nanoparticle surface, their Raman scattering signals are amplified due to a strong localized optical field. Thus, the uniform electric field enhancement in NPA ensures a high sensitivity of SERS detection in low concentration solution.

The geometric deviation of NPA is inevitable due to the limitation of processing accuracy, which prompted us to investigate the effects of printing deviation on field enhancement. The linear profiles of the electric field intensity $|E|/|E_0|$ along the X-axis in the XY-plane, illustrated by the dotted black line in figure 4(b), are shown in figures 4(g)–(i). Compared

with the single particle, the enhancement of nanoparticles was more pronounced (figure 4(g)). The enhancement difference between profiles with various pitches p is negligible (figure 4(g)), suggesting the enhancement is insensitive to pitch deviation in 10 nm. This inference is also supported by the profiles in the XZ plane (figure S7(a)). The field profiles of different particle radii were not coincident, as illustrated in figure 4(g). The enhancement is strongest for a radius of 91 nm, which is the most desired value for our purpose. The variation of maximum $|E|/|E_0|$ was smaller than 0.5 (figure 4(g)) when the radius deviation was less than 10 nm. Whereas the maximum etching error of FIB processing is <8 nm [28], indicating the influence of radius deviation is inappreciable. We also noticed that the enhancement went down rapidly as radius r increases (figure S7(b)). Additionally, the maximum $|E|/|E_0|$ will be delocalized when the radius r is too large. The surface area of each particle would also expand with the increasing r . Thus, a remarkable enhancement reduction of the NPA with a sizeable r will not be expected. As the embedded depth h varies, the difference between $|E|/|E_0|$ profiles in the XY-plane is also inconspicuous (figure 4(i)), although the increasing depth h resulted in an overall decrease in $|E|/|E_0|$ in the XZ-plane (figure S7(c)). The enhancement will be reduced to nearly zero if the nanoparticles are fully buried in PDMS. Thus, the h value should be slightly higher than r value to reach an outstanding detection enhancement and reliability.

3.3. Stability and sensitivity of repeated SERS detection

The NPA-based SERS strips were cleaned and used repeatedly to test their stability and sensitivity. The strips fabricated with different laser energy were subjected to successive 2 min of rinsing, 7 h of soaking in deionized water, 5 min of ultrasonic cleaning, and 10 min of drying at 65 °C, as shown in figure 5(a). After the continuous treatments, a few nanoparticles fell off the PDMS substrate due to their smaller embedded depth under a lower laser fluence, as shown in figure 5(b). When the pulse energy exceeds 7.55 μJ , the microscopic morphology and alignment consistency of NPA will not be damaged by the above-mentioned cleaning, as shown in figure 5(c), indicating a reusable feature of our SERS strip. The MG may stay on the array surface (figure 5(d)) and cannot be removed by a prolonged washing (figure 5(e)). We found that the oxidizing reagent could clean the MG residues via the redox reaction. Figure 5(f) shows the Raman spectrum tested by a used SERS strip after soaking in 5% NaClO solution for 5 min, where all the characteristic peaks of MG disappeared entirely. Therefore, a protocol for reusing the nanoparticle test strip was developed, as demonstrated in figure 5(g). The workflow is as follows: ① soak the used strip in 5% NaClO solution for 5 min to clean MG residues; ② ultrasonic clean with deionized water for 10 min to remove NaClO; ③ dry at 65 °C to accelerate the decomposition of NaClO residues; ④ re-add the

MG solution; ⑤ carry out the Raman test. An alternative detection method of high and low concentrations (10^{-6} mol·l $^{-1}$ and 10^{-11} mol·l $^{-1}$) of MG solutions was performed to investigate the sensitivity variation. As shown in figure 5(h), the 1619 cm^{-1} peak intensities obtained after a dozen replicates were precisely coincident, even if the solution concentration has five orders of magnitude differences. Besides, the relative standard deviation (figure 5(i)) also did not vary conspicuously, undergoing our continual repeats.

Generally, the analyte residue is tough to remove altogether for the common SERS substrates because their micro-nano structures are irregular and highly fragile [46]. A long time of physical and chemical cleaning will destroy the plasmonic enhancement and weaken the detecting sensitivity. The reasonable embedded depth of each nanoparticle and the smooth topography of the entire array make our SERS strip stable and reusable while maintaining a high sensitivity, which could not be achieved by the direct laser structuring approaches.

3.4. In-situ reaction monitoring in microfluidic chip

Thanks to the high stability and sensitivity, the SERS strip was combined with the microfluidic chip to detect chemical reactions online. The designed microfluidic SERS chip consists of a glass plate etched with microchannel and microchamber and a PDMS film embedded with NAPs (figure 6(a)). The microfluidic chip is placed on the moving stage of Raman microscope. The NPAs can be observed through a viewing window on the microchamber (figure 6(a)). The microfluidic device is presented in figure 6(b). Two injectors are used for storage and infusion of the reaction liquids. The MG and NaClO solutions are injected through the inlets on both sides and mixed in the middle reaction chamber through the microchannel. The variation of substances during the redox reaction will be captured by the SERS spectrum.

Figure 6(c) presents the Raman spectra of MG and NaClO solution with different proportions after a thorough reaction. As the ratio of NaClO solution increases, the Raman intensity exhibits a noticeable decline, indicating the MG concentration of the mixture decreases after the reaction. The trend of the 1619 cm^{-1} peak intensity towards several ratio set-ups is plotted in figure 6(d) (right axis). The corresponding MG concentration is derived from the fitted equation (figure 6(d)). In addition, the temporal Raman spectra of a 1:1 ratio of MG/NaClO were also measured, as shown in figure 6(e). The spectral intensity decreases over time. The time dependence of MG concentration in figure 6(f) demonstrates that the reaction rate rapidly decreases with the reaction proceeding. Moreover, the lower the NaClO proportion in the initial mixture, the more slowly the redox will proceed. The 1619 cm^{-1} peak indicates a vibration mode of three phenyl rings (figure 6(g)) [40]. A possible reaction route between MG and NaClO is charted in figure 6(g). Hypochlorite ion (ClO^-) is produced from

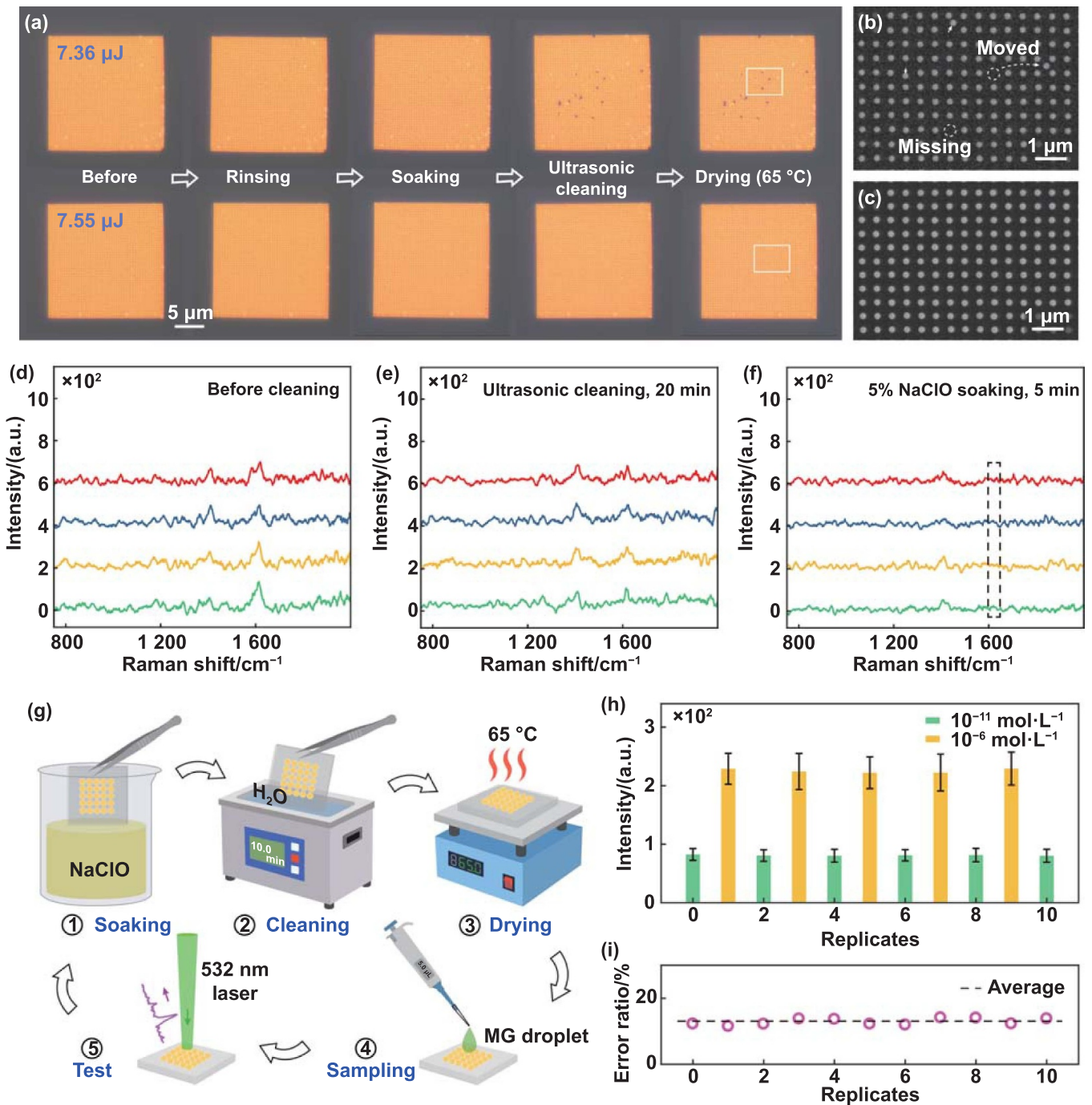


Figure 5. Reliability testing of nanoparticle array for SERS application. (a) Optical images of NPs prepared with different pulse energies after successive treatments: rinsing, soaking, ultrasonic cleaning, and drying. SEM images of the (b) damaged and (c) undamaged NPs after the above treatments. The enlarged areas are illustrated with the white box in (a). Raman spectra of residues on a used array ($10^{-6} \text{ mol}\cdot\text{l}^{-1}$ MG test) (d) before cleaning, after (e) ultrasonic cleaning for 25 min, and (f) soaking for 5 min with 5% NaClO solution. (g) A schematic of the reuse process of the SERS strip. (h) Peak (1619 cm^{-1}) intensity and (i) relative standard deviation of alternately measured $10^{-11} \text{ mol}\cdot\text{l}^{-1}$ and $10^{-6} \text{ mol}\cdot\text{l}^{-1}$ MG solutions.

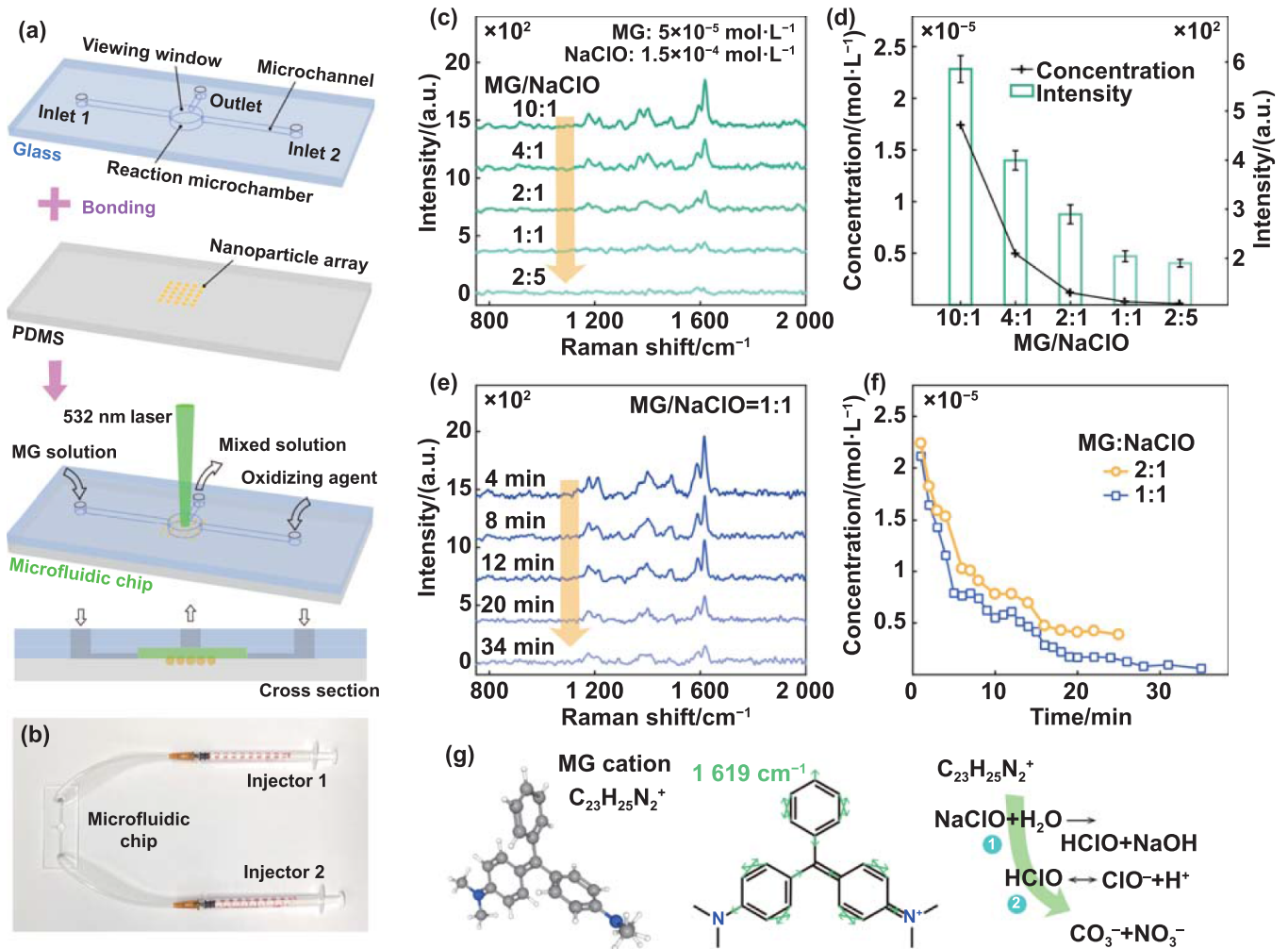


Figure 6. In-situ monitoring of concentration variation during oxidation. (a) Schematic of the creation of a microfluidic SERS chip. (b) Microfluidic device with SERS-active nanoparticle arrays. (c) Raman spectra for mixed solutions with different proportions of MG ($5 \times 10^{-5} \text{ mol}\cdot\text{l}^{-1}$)/NaClO ($1.5 \times 10^{-4} \text{ mol}\cdot\text{l}^{-1}$) after a full reaction. (d) Variation of MG concentration and peak (1619 cm^{-1}) intensity (right axis) with several MG/NaClO ratio set-ups. (e) Raman spectra of mixed solution (MG/NaClO = 1:1) at different times. (f) Time dependence of MG concentration with different mixing ratios. (g) MG geometry, phenyl ring vibration mode, and possible redox route between MG^+ and ClO^- .

the reaction of NaClO and H_2O , making the MG oxidation degradation. The disappearance of 1619 cm^{-1} peak reveals that the phenyl rings are completely destroyed within tens of minutes during this redox process, which is different from the electrochemical oxidation [47]. Overall, combining our NPA-based SERS strip with the microfluidic chip provides an effective approach to investigating the micro-reaction processes online.

4. Conclusions

In summary, femtosecond laser-induced nanoparticle implantation on flexible polymer film was used to fabricate microfluidic SERS substrates with excellent sensitivity and reusability. The uniformity and accuracy of printed NPA on PDMS were remarkably improved using our polarization-modulated method. The position deviation of nanoparticles

was reduced to 3% of the arrangement pitch, ensuring a significant electromagnetic field enhancement introduced by the surface plasmonic resonances. The implanted Au-NPA strips were successfully used to quantify the MG solution of low concentration directly and achieved a detection limit lower than 10 ppt and enhancement factor exceeded 9×10^8 , much better than most microfluidic SERS substrates. Benefiting from the uniform embedment of laser-implanted nanoparticles on the flexible substrate, our SERS strips were highly robust, difficult to damage through physical and chemical cleaning. The sensitivity and reproducibility were well maintained after repeated SERS detection, exhibiting remarkable reusability that is impossible for most laser-prepared methods. Eventually, NPAs were integrated into the microfluidic chip, and the oxidation reaction between MG/NaClO reactants was monitored online. Compared with other laser-prepared nanostructures, laser-induced implanted nanoparticles on the flexible substrate represented high consistency, robustness, and

applicability. This paves a new way for high-performance and low-cost microfluidic SERS detection.

In the future, we will focus on the multiple laser-induced transfer technique for the same substrate to further enhance plasmon resonance and improve SERS sensitivity.

Acknowledgments

Y X Hu and Y Zhou contributed equally to this work. The authors would like to acknowledge the support from the National Natural Science Foundation of China (Grant Numbers: U21A20135 and 52205488), ‘Shuguang Program’ supported by Shanghai Education Development Foundation and Shanghai Municipal Education Commission (Grant Number: 20SG12), and Shanghai Jiao Tong University (Grant Number: 2020QY11).

ORCID iDs

Yongxiang Hu  <https://orcid.org/0000-0003-2704-3521>

Yu Zhou  <https://orcid.org/0000-0002-0499-6891>

References

- [1] Xu K, Zhou R, Takei K and Hong M 2019 Toward flexible surface-enhanced Raman scattering (SERS) sensors for point-of-care diagnostics *Adv. Sci.* **6** 1900925
- [2] Lin X, Lin D, Chen Y, Lin J, Weng S, Song J and Feng S 2021 High throughput blood analysis based on deep learning algorithm and self-positioning super-hydrophobic SERS platform for non-invasive multi-disease screening *Adv. Funct. Mater.* **31** 2103382
- [3] Sugioka K 2019 Hybrid femtosecond laser three-dimensional micro- and nanoprocessing: a review *Int. J. Extrem. Manuf.* **1** 012003
- [4] AbdElFatah T et al 2023 Nanoplasmonic amplification in microfluidics enables accelerated colorimetric quantification of nucleic acid biomarkers from pathogens *Nat. Nanotechnol.* **18** 1–11
- [5] Yang Y, Li J, Luo J, Ding Y and Song P 2022 Effect of surface hydroxyls and porous nanostructured sensors integrated for SERS monitoring and efficient removal of organic pollutants *Appl. Surf. Sci.* **601** 154123
- [6] Zhang K, Li H, Wang W, Cao J, Gan N and Han H 2020 Application of multiplexed aptasensors in food contaminants detection *ACS Sens.* **5** 3721–38
- [7] Pu H, Xiao W and Sun D-W 2017 SERS-microfluidic systems: a potential platform for rapid analysis of food contaminants *Trends Food Sci. Technol.* **70** 114–26
- [8] Chrimes A F, Khoshmanesh K, Stoddart P R, Mitchell A and Kalantar-Zadeh K 2013 Microfluidics and Raman microscopy: current applications and future challenges *Chem. Soc. Rev.* **42** 5880–906
- [9] Zhou W and Odom T W 2011 Tunable subradiant lattice plasmons by out-of-plane dipolar interactions *Nat. Nanotechnol.* **6** 423–7
- [10] Baca A J, Montgomery J M, Cambrea L R, Moran M, Johnson L, Yacoub J and Truong T T 2011 Optimization of nanopost plasmonic crystals for surface enhanced Raman scattering *J. Phys. Chem. C* **115** 7171–8
- [11] Aksu S, Huang M, Artar A, Yanik A A, Selvarasah S, Dokmeci M R and Altug H 2011 Flexible plasmonics on unconventional and nonplanar substrates *Adv. Mater.* **23** 4422–30
- [12] Zhan H, Cheng F, Chen Y, Wong K W, Mei J, Hui D, Lau W M and Liu Y 2016 Transfer printing for preparing nanostructured PDMS film as flexible SERS active substrate *Composites B* **84** 222–7
- [13] Guo J, Zeng F, Guo J and Ma X 2020 Preparation and application of microfluidic SERS substrate: challenges and future perspectives *J. Mater. Sci. Technol.* **37** 96–103
- [14] Yu J, Wu J, Yang H, Li P, Liu J, Wang M, Pang J, Li C, Yang C and Xu K 2022 Extremely sensitive SERS sensors based on a femtosecond laser-fabricated superhydrophobic/-philic microporous platform *ACS Appl. Mater. Interfaces* **14** 43877–85
- [15] Yang H, Guan X, Pang G, Zheng Z, Li C, Yang C, Wang M and Xu K 2021 Femtosecond laser patterned superhydrophobic/hydrophobic SERS sensors for rapid positioning ultratrace detection *Opt. Express* **29** 16904–13
- [16] Bai S and Sugioka K 2021 Recent advances in the fabrication of highly sensitive surface-enhanced Raman scattering substrates: nanomolar to attomolar level sensing *Light Adv. Manuf.* **2** 186–210
- [17] B-B X, Z-C M, Wang L, Zhang R, Niu L-G, Yang Z, Zhang Y-L, Zheng W-H, Zhao B and Xu Y 2011 Localized flexible integration of high-efficiency surface enhanced Raman scattering (SERS) monitors into microfluidic channels *LChip* **11** 3347–51
- [18] Bai S, Serien D, Hu A and Sugioka K 2018 3D microfluidic Surface-Enhanced Raman Spectroscopy (SERS) chips fabricated by all-femtosecond-laser-processing for real-time sensing of toxic substances *Adv. Funct. Mater.* **28** 1706262
- [19] Ma Z C, Zhang Y L, Han B, Liu X Q, Zhang H Z, Chen Q D and Sun H B 2017 Femtosecond laser direct writing of plasmonic Ag/Pd alloy nanostructures enables flexible integration of robust SERS substrates *Adv. Mater. Technol.* **2** 1600270
- [20] Han B, Zhang Y-L, Zhu L, Chen X-H, Ma Z-C, Zhang X-L, Wang J-N, Wang W, Liu Y-Q and Chen Q-D 2018 Direct laser scribing of AgNPs@ RGO biochip as a reusable SERS sensor for DNA detection *Sens. Actuators B* **270** 500–7
- [21] Lao Z, Zheng Y, Dai Y, Hu Y, Ni J, Ji S, Cai Z, Smith Z J, Li J and Zhang L 2020 Nanogap plasmonic structures fabricated by switchable capillary-force driven self-assembly for localized sensing of anticancer medicines with microfluidic SERS *Adv. Funct. Mater.* **30** 1909467
- [22] Huang Y, Li Y, Pan K, Fang Y, Chan K C, Xiao X, Wei C, Novoselov K S, Gallop J and Hao L 2023 A direct laser-synthesized magnetic metamaterial for low-frequency wideband passive microwave absorption *Int. J. Extrem. Manuf.* **5** 035503
- [23] Lee S J, Lee H, Begildayeva T, Yu Y, Theerthagiri J, Kim Y, Lee Y W, Han S W and Choi M Y 2022 Nanogap-tailored Au nanoparticles fabricated by pulsed laser ablation for surface-enhanced Raman scattering *Biosens. Bioelectron.* **197** 113766
- [24] Zhang D, Liu R and Li Z 2021 Irregular LIPSS produced on metals by single linearly polarized femtosecond laser *Int. J. Extrem. Manuf.* **4** 015102
- [25] Kuznetsov A I, Evlyukhin A B, Gonçalves M R, Reinhardt C, Koroleva A, Arnedillo M L, Kiyani R, Marti O and Chichkov B N 2011 Laser fabrication of large-scale nanoparticle arrays for sensing applications *ACS Nano* **5** 4843–9
- [26] Zacharatos F, Duderstadt M, Almpanis E, Patsiouras L, Kurselis K, Tsoukalas D, Reinhardt C, Papanikolaou N, Chichkov B N and Zergioti I 2021 Laser printing of Au nanoparticles with sub-micron resolution for the fabrication of monochromatic reflectors on stretchable substrates *Opt. Laser Technol.* **135** 106660

- [27] Li M, Zhao F, Zeng J, Qi J, Lu J and Shih W-C 2014 Microfluidic surface-enhanced Raman scattering sensor with monolithically integrated nanoporous gold disk arrays for rapid and label-free biomolecular detection *J. Biomed. Opt.* **19** 111611
- [28] Zhou Y, Luo G, Hu Y, Wu D, Hu C and Qu M 2023 Femtosecond laser printing patterned nanoparticles on flexible substrate by tuning plasmon resonances via polarization modulation *Int. J. Mach. Tool Manuf.* **189** 104040
- [29] Liu R, Zha Z, Li C, Shafi M, Peng Q, Liu M, Zhang C, Du X and Jiang S 2021 Coupling of multiple plasma polarization modes in particles-multilayer film system for surface-enhanced Raman scattering *APL Photonics* **6** 036104
- [30] Liu R, Jiang L, Lu C, Yu Z, Li F, Jing X, Xu R, Zhou W and Jin S 2020 Large-scale two-dimensional titanium carbide MXene as SERS-active substrate for reliable and sensitive detection of organic pollutants *Spectrochim. Acta A* **236** 118336
- [31] Zeng Z, Liu Y and Wei J 2016 Recent advances in surface-enhanced Raman spectroscopy (SERS): finite-difference time-domain (FDTD) method for SERS and sensing applications *TRAC Trends Anal. Chem.* **75** 162–73
- [32] Johnson P B and Christy R-W 1972 Optical constants of the noble metals *Phys. Rev. B* **6** 4370
- [33] Schneider F, Draheim J, Kamberger R and Wallrabe U 2009 Process and material properties of polydimethylsiloxane (PDMS) for Optical MEMS *Sens. Actuators A* **151** 95–99
- [34] Xiong L, Chen P and Zhou Q 2014 Adhesion promotion between PDMS and glass by oxygen plasma pre-treatment *J. Adhes. Sci. Technol.* **28** 1046–54
- [35] Luo G, Wu D, Zhou Y, Hu Y and Yao Z 2022 Elucidating ejection regimes of metal microdroplets in voxel-based laser-induced forward transfer *Addit. Manuf.* **55** 102814
- [36] Moon H-Y, Sidhu M S, Lee H S and Jeoung S C 2015 Dynamic changes in PDMS surface morphology in femtosecond laser treatment *Opt. Express* **23** 19854–62
- [37] Struleva E V, Komarov P S and Ashitkov S I 2019 Comparison of femtosecond laser ablation of gold and nickel *High Temp.* **57** 659–62
- [38] Wang D, Guan J, Hu J, Bourgeois M R and Odom T W 2019 Manipulating light-matter interactions in plasmonic nanoparticle lattices *Acc. Chem. Res.* **52** 2997–3007
- [39] Yang A, Hryn A J, Bourgeois M R, Lee W-K, Hu J, Schatz G C and Odom T W 2016 Programmable and reversible plasmon mode engineering *Proc. Natl Acad. Sci.* **113** 14201–6
- [40] Schneider S, Brehm G and Freunsch P 1995 Comparison of Surface-Enhanced Raman and Hyper-Raman Spectra of the Triphenylmethane Dyes Crystal Violet and Malachite Green *Phys. Status Solidi b* **189** 37–42
- [41] Lee S, Choi J, Chen L, Park B, Kyong J B, Seong G H, Choo J, Lee Y, Shin K-H and Lee E K 2007 Fast and sensitive trace analysis of malachite green using a surface-enhanced Raman microfluidic sensor *Anal. Chim. Acta* **590** 139–44
- [42] Quang L X, Lim C, Seong G H, Choo J, Do K J and Yoo S-K 2008 A portable surface-enhanced Raman scattering sensor integrated with a lab-on-a-chip for field analysis *LChip* **8** 2214–9
- [43] Zhang W, Li B, Chen L, Wang Y, Gao D, Ma X and Wu A 2014 Brushing, a simple way to fabricate SERS active paper substrates *Anal. Methods* **6** 2066–71
- [44] Luo X, Pan R, Cai M, Liu W, Chen C, Jiang G, Hu X, Zhang H and Zhong M 2021 Atto-Molar Raman detection on patterned superhydrophilic-superhydrophobic platform via localizable evaporation enrichment *Sens. Actuators B* **326** 128826
- [45] Zhang S, Mao N, Wu J, Tong L, Zhang J and Liu Z 2017 In-plane uniaxial strain in black phosphorus enables the identification of crystalline orientation *Small* **13** 1700466
- [46] Li Z, Huang X and Lu G 2020 Recent developments of flexible and transparent SERS substrates *J. Mater. Chem. C* **8** 3956–69
- [47] Singh S, Lo S L, Srivastava V C and Hiwarkar A D 2016 Comparative study of electrochemical oxidation for dye degradation: parametric optimization and mechanism identification *J. Environ. Chem. Eng.* **4** 2911–21